AIAA AVIATION Forum
12-16 June 2023, San Diego, CA and Online
AIAA AVIATION 2023 Forum

10.2514/6.2023-4452

An Aeroelastic Flight Dynamics Model for Gust Load Alleviation of Energy-Efficient Passenger Airplanes

Yannic Beyer*, Davide Cavaliere†, Kjell Bramsiepe‡, Khalid Khalil§, André Bauknecht¶, Nicolas Fezans‖, Meiko Steen**, Peter Hecker††
Technische Universität Braunschweig, Cluster of Excellence SE²A – Sustainable and Energy-Efficient Aviation, Hermann-Blenk-Str. 42, 38108 Braunschweig, Germany.

Gust load alleviation (GLA) can reduce the maximum loads encountered by airplanes, allowing the structure to be designed lighter, thus saving fuel. Active GLA therefore represents an important subarea in the research of energy-efficient passenger airplanes. However, from a flight dynamics perspective, there are no publicly available simulation environments that allow for an efficient and modular investigation of different technologies like novel GLA controllers or novel flow actuators. Therefore, this paper presents such a simulation environment. The presented aeroelastic flight dynamics model is based on indicial functions combined with a dynamic stall model to predict the unsteady aerodynamics similar to a strip theory approach, while the downwash is considered using a nonlinear steady lifting line method. The structural dynamics are based on the mode displacement method and coupled with the aerodynamics model using constant transformation matrices as well as nonlinear transformations for the inflow. A comparison of the presented model with unsteady Reynolds-Averaged Navier–Stokes simulations shows good agreement for a selected gust case. The presented simulation model is parameterized as an energy-efficient passenger airplane with a light-weight wing sizing by reducing the limit loads from 2.5 g to 2.0 g for equivalent pull-up maneuvers. Open-loop gust load envelopes are presented and discussed for the energy-efficient airplane with different model settings, e.g. with and without dynamic stall model. The source code of the simulation modules is available at: `https://github.com/iff-gsc/se2a_aviation_2023`. A video of the flight simulation is available at: `https://youtu.be/cO5q06Qkkgk`

I. Introduction

When certifying commercial aircraft, evidence must be provided that the structure can withstand strong turbulence and gusts in addition to a set of maneuver cases [1, 2]. The high loads occurring in such situations require that the structure, especially the wings, must be sized accordingly. This is accompanied by a rather high structural weight or by compromises in other design features (e.g. the 'triangular' lift distribution of the Boeing 747 [3]), which results in additional fuel consumption. In order to improve efficiency, technologies are being researched that keep the loads as low as possible. Simulation models based on various methods are used to calculate these loads. The models typically consist of unsteady aerodynamic models coupled with elastic structural models. Different methods with varying levels of accuracy are available for both the aerodynamic models and the structural models, whereby the computational effort typically increases with the model quality [4].

In flight dynamics modeling, a compromise between accuracy and simulation speed must be found, as it is often required that the simulation can be run in real time on a contemporary desktop computer. Typical models from this application area are the Cranfield Aircraft Accelerated Loads Model (CA^2LM) framework [4–6] and the University of Michigan's Nonlinear Aeroelastic Simulation Toolbox (UM/NAST) [7–9]. However, both of these models are closed source. While the CA^2LM framework is used for commercial aircraft with moderate flexibility, the UM/NAST toolbox is used for highly flexible unmanned aircraft.

*PhD Researcher, Technische Universität Braunschweig, Institute of Flight Guidance, 38108 Braunschweig, Germany.
†PhD Researcher, DLR (German Aerospace Center), Institute of Flight Systems, 38108 Braunschweig, Germany.
‡PhD Researcher, DLR (German Aerospace Center), Institute of Aeroelasticity, 37073 Göttingen, Germany.
§PhD Researcher, Technische Universität Braunschweig, Institute of Fluid Mechanics, 38108 Braunschweig, Germany.
¶Junior Research Group Leader, Technische Universität Braunschweig, Institute of Fluid Mechanics, 38108 Braunschweig, Germany.
‖Scientific Advisor, DLR (German Aerospace Center), Institute of Flight Systems, 38108 Braunschweig, Germany.
**Workgroup Leader, Technische Universität Braunschweig, Institute of Flight Guidance, 38108 Braunschweig, Germany.
††Professor and Head of Institute, Technische Universität Braunschweig, Institute of Flight Guidance, 38108 Braunschweig, Germany.

For moderate flexibility, linear structural models can be used, while for high flexibility, nonlinear and thus more computationally expensive models must be used. The simplest form of flexible aircraft equations of motion is the addition of a linear structural dynamics model to the rigid-body equations of motion when inertial coupling is neglected [10]. This model can be extended by several terms of the inertial couplings [11]. Nonlinear structural models for highly flexible aircraft are described in [12].

Aerodynamics models range from Modified Strip Theory (MST) [13] to potential theory models such as the Doublet Lattice Method (DLM) and the Unsteady Vortex Lattice Method (UVLM) to Computational Fluid Dynamics (CFD) methods [4, 14]. CFD models, such as the Unsteady Reynolds-Averaged Navier–Stokes (URANS) simulation models [15] are only used at selected operating points due to the very high computational cost. MST is implemented in both CA^{2}LM and UM/NAST and used in other publications [16–18]. In addition to the low computational cost, MST has the advantage over DLM and UVLM that dynamic stall [19, 20] can be considered. CFD studies of gust interactions of rigid and unaccelerated aircraft have shown that dynamic stall may have a significant effect on loads [15, 21, 22]. However, it is questionable whether a similar quality as with DLM and UVLM can be achieved with MST for the spanwise lift distribution. At least in the stated publications on MST, the aerodynamic models are not validated in this respect. In [23], a model is presented that fills this gap. The model is called Nonlinear Indicial Functions Lifting Line (NL-IF-LL) and exhibits a valid spanwise lift distribution for wings with moderate to high aspect ratio.

A. Energy-Efficient Airplane

One of the three research areas of the SE^{2}A (Sustainable and Energy-Efficient Aviation) Cluster of Excellence investigates the potential of promising aircraft technologies to decrease the fuel consumption and environmental impact of future passenger airplanes. A central methodology in this research framework is the conceptual aircraft design, which makes assumptions about these technologies in order to optimize the design parameters and predict the potential savings in fuel consumption. When all technologies are combined, the predicted fuel consumption of a generic mid-range (MR) aircraft, see Fig. 1a, is about 30% – 40% less than that of current comparable aircraft [24].

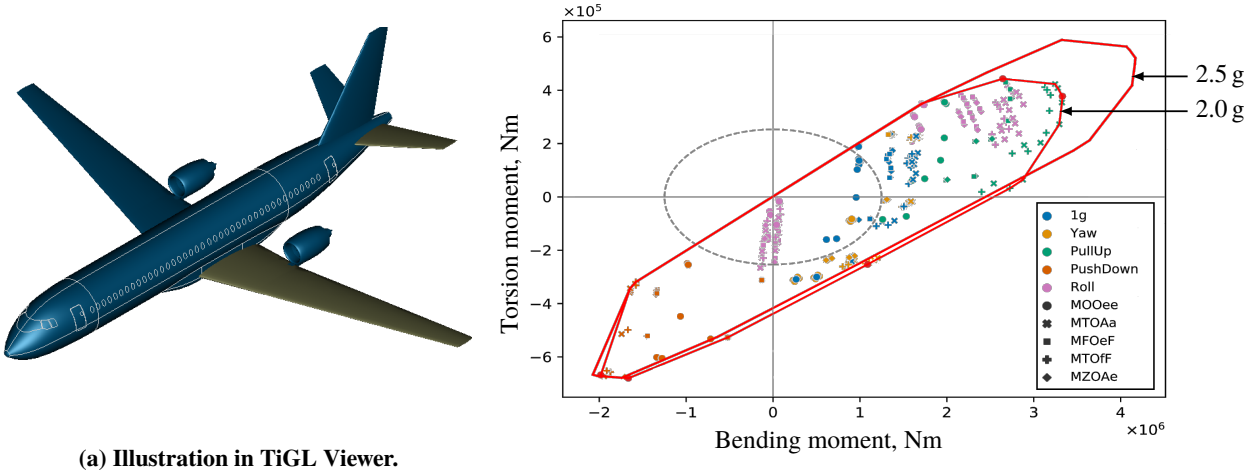

(a) Illustration in TiGL Viewer.

(b) Sizing load envelopes at the wing root

Fig. 1 SE^{2}A Mid-Range (MR) Aircraft.

The resulting SE^{2}A MR design is comparable in size and capabilities to an Airbus A320-200, and is designed considering the use of ultra-high bypass ratio engines, laminar flow control, advanced materials, and load alleviation technologies. The design optimization aims to balance direct operating costs against CO_2-equivalent emissions (including contrail effects), and therefore has a relatively low and slow design point of 7650 m altitude and Mach 0.71. The resulting design features include over-wing engine mounts, increased wingspan and aspect ratio, and a relatively low wing sweep. The complete aircraft design, along with several other variants, is thoroughly described in [24].

Table 1 summarizes characteristic masses and airspeeds of the SE^{2}A MR design, and Fig. 2 illustrates the related flight envelope. These values do not reflect a detailed design, but are instead derived from the conceptual design phase and are used as reference for, e.g., computing load cases according to the certification specifications. M_D and V_D, for example, roughly correspond to the minimal conditions laid out in CS25.335/AMC25.335(b)(2) [1], and may not

Table 1 SE^{2}A MR characteristic quantities

Parameter	Value
V_{s1g}	76 m/s EAS
V_C / M_C	177 m/s EAS / M0.77
V_D / M_D	192 m/s EAS / M0.85
MTOW	64 158 kg
MZFW	55 771 kg
MLW	57 742 kg
z_{MO}	11 200 m

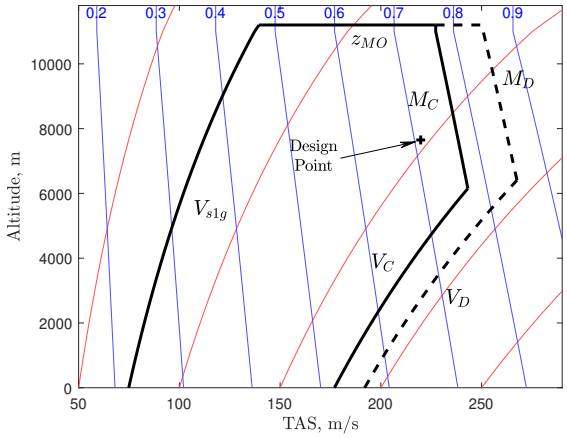

Fig. 2 SE^{2}A MR flight envelope. Red lines are iso-EAS and blue lines are iso-Mach.

comply with the full scope of the certification specifications.

A detailed FEM model of the MR aircraft was generated with the DLR design-process *cpacs-MONA* [25]. The design load cases in this research are reduced to a set of maneuver load cases within the design process for simplification (pull-ups, push-downs, yaw, roll, and cruise flight). Gust load cases are neglected to take comprehensive GLA into account. Two sizing cases are applied by assuming either a 2.5 g or a reduced 2.0 g load factor for the pull-up maneuver load cases. In doing so, the root bending moment is reduced to an equivalent root bending moment which could be achieved with intense MLA and GLA. Note that this approach neglects the increase in torsional loads typically seen when using wing control surfaces for active load alleviation [26]. Figure 1b illustrates the wing sizing approach for the reduced loads from 2.5 g to 2.0 g. This results in a 5.3% reduction in the primary structural mass of the wing.

B. Contributions

This work firstly contributes a new open source method and secondly contributes results for the energy-efficient airplane, see Fig. 1a, as described below.

In Section II a reduced-order aeroelastic flight dynamics model is presented. The methodological contribution includes the coupling of the aerodynamic model presented in [23] with a linear structural model. For this purpose, the novel aerodynamics model from [23] is briefly summarized and the coupling is described in detail. The model is implemented in Matlab/Simulink and the source code is freely available. It is suitable for slightly to moderately flexible aircraft at sub- and transonic speeds and includes dynamic stall. In the future, this model can be used to design and simulate novel active gust load alleviation systems.

The presented model is applied to the presented energy-efficient aircraft, see Fig. 1a. First, results of the NL-IF-LL aerodynamic model are briefly compared with URANS results in Section III.B. Then, the flight characteristics of the aircraft are briefly discussed. Finally, the aircraft's load envelopes for discrete 1–cos gusts are presented in Section III. Here, the differently sized wings are compared. Moreover, the effect of stall on the gust loads is presented.

II. Reduced-Order Aeroelastic Flight Dynamics Model

An overview of the reduced-order aeroelastic flight dynamics model is shown in Fig. 3. The most important component of the model is the aerodynamics model, which is coupled with a structural dynamics model and the equations of motion. The aerodynamics model is described and validated in detail in [23] and briefly summarized in Section II.A. In Section II.B the structural dynamics model is presented. Then, the flexible-body equations of motion are described in Section II.C. In the next Section II.D, the coupling between the aerodynamic model and the flexible-body equations of motion is presented in detail. We also discuss the trimming and linearization of the overall model in Section II.E.

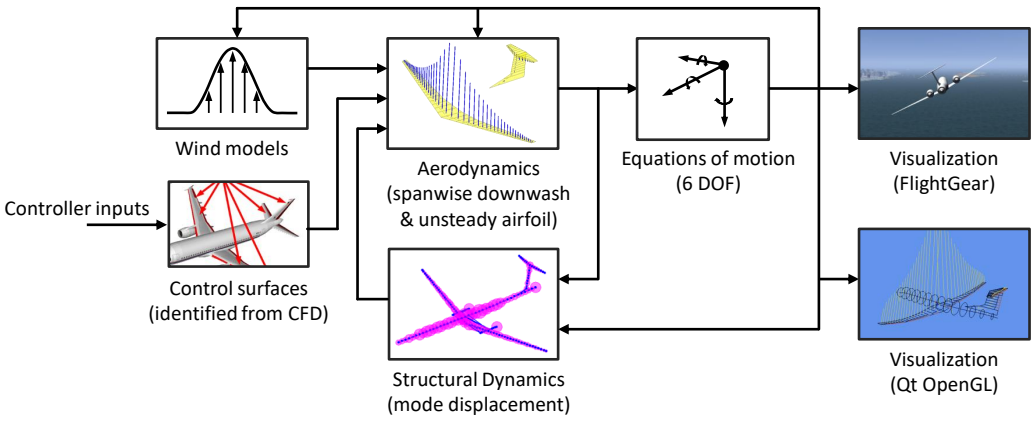

Fig. 3 Overview of the flight dynamics simulation framework mainly implemented in MATLAB/Simulink [27].

A. Aerodynamics Model

As can be seen in Fig. 3, each wing of the aircraft is divided into several strips. For each strip i there is a separate unsteady airfoil model based on the concept of indicial functions. An overview of the aerodynamics model is shown in Fig. 4. It consists of an unsteady airfoil model, see Section II.A.1, a dynamic stall model, see Section II.A.2 and a spanwise downwash model, see Section II.A.3.

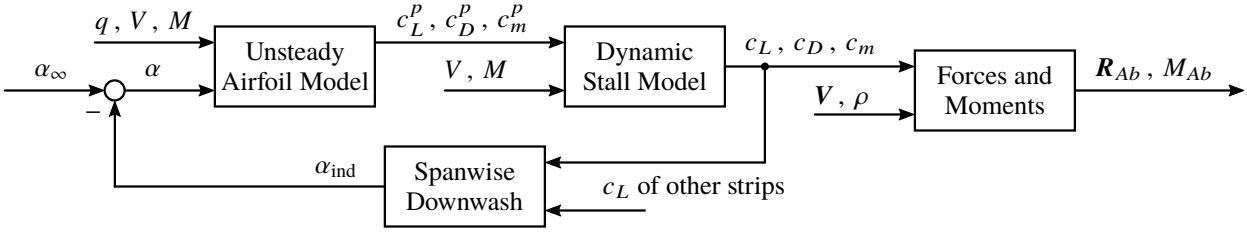

Fig. 4 Overview of nonlinear unsteady airfoil model with spanwise downwash coupling. The index i has been omitted for simplicity.

1. Unsteady airfoil model

The concept of indicial lift functions is based on the approximation of the Wagner function with exponential functions. This applies to incompressible flow. For compressible flow up to the transonic Mach numbers, a Mach number dependent approximation of has been published in [28]. It is formulated as a state space model:

$$\dot{\boldsymbol{x}} = \boldsymbol{A}\boldsymbol{x} + \boldsymbol{B}\begin{bmatrix}\alpha & q\end{bmatrix}^T \tag{1}$$

$$\begin{bmatrix}c_L^p & c_D^p & c_m^p\end{bmatrix}^T = \boldsymbol{C}\boldsymbol{x} + \boldsymbol{D}\begin{bmatrix}\alpha & q\end{bmatrix}^T \tag{2}$$

This model includes two inputs, the angle of attack at 1/4 chord α and the dimensionless pitch rate q, two outputs, the lift coefficient $c_L^p = c_L^{\text{c}} + c_L^{\text{nc}}$ and the pitching moment coefficient c_m^p, and eight states $\boldsymbol{x}$. The matrices $\boldsymbol{A}$, $\boldsymbol{B}$, $\boldsymbol{C}$ and $\boldsymbol{D}$ depend on the velocity relative to the chord, Mach number, aerodynamic center and lift curve slope. For details, please refer to [28]. From the circulatory part of the unsteady lift coefficient c_L^{c} the effective angle of attack α_E can be computed [19, 23].

It is important to note that the model shown in Eqs. (1) and (2), as defined in [28], yields meaningful results only if the velocity is constant, due to unfavorable definition of the state variables $\boldsymbol{x}$. This can lead to erroneous flutter in an aeroelastic flight dynamics simulation. The problem can be solved by a more suitable definition of the state variables:

$$\tilde{\boldsymbol{x}} = \boldsymbol{T}\boldsymbol{x} \quad \text{with} \quad \boldsymbol{T} = \boldsymbol{A} \tag{3}$$

From this follows a transformed state space model:

$$\dot{\tilde{\boldsymbol{x}}} = \tilde{\boldsymbol{A}}\tilde{\boldsymbol{x}} + \tilde{\boldsymbol{B}} \begin{bmatrix} \alpha & q \end{bmatrix}^T \tag{4}$$

$$\begin{bmatrix} c_L^p & c_D^p & c_m^p \end{bmatrix}^T = \tilde{\boldsymbol{C}}\tilde{\boldsymbol{x}} + \tilde{\boldsymbol{D}} \begin{bmatrix} \alpha & q \end{bmatrix}^T \tag{5}$$

with $\tilde{\boldsymbol{A}} = \boldsymbol{T}\boldsymbol{A}\boldsymbol{T}^{-1}$, $\tilde{\boldsymbol{B}} = \boldsymbol{T}\boldsymbol{B}$, $\tilde{\boldsymbol{C}} = \boldsymbol{C}\boldsymbol{T}^{-1}$ and $\tilde{\boldsymbol{D}} = \boldsymbol{D}$, where $\tilde{\boldsymbol{A}} = \boldsymbol{A}$.

2. Dynamic Stall Model

The linear model for the unsteady airfoil coefficients, presented in Eqs. (1) and (2), can be extended by a nonlinear model for the consideration of dynamic stall [19, 20]. For this, steady-state lift coefficients with stall are required. For the presented energy-efficient airplane, the nonlinear steady-state lift coefficients are shown in Fig. 5 as a function of Mach number.

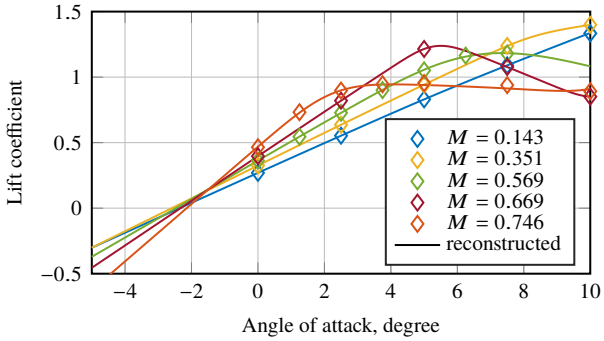

Fig. 5 Steady F15 airfoil lift coefficient model based on steady RANS data for multiple Mach numbers [27].

For this purpose, the stationary (exponent 'st') flow separation point relative to the airfoil chord length is calculated as a function of the lift coefficient [20]:

$$f^{\mathrm{st}}(\alpha) = \left(2\sqrt{\frac{c_L^{\mathrm{st}}(\alpha)}{c_{L\alpha}(\alpha - \alpha_0)}} - 1 \right)^2 \tag{6}$$

with the zero lift angle of attack α_0 and the lift curve slope

$$c_{L\alpha} = \max\left(c_L^{\mathrm{st}}(\alpha)/(\alpha - \alpha_0) \right) \tag{7}$$

The trailing-edge separation model adds two states to the airfoil model. The first state is a delay (modeled as a first-order low-pass filter) of the linear lift coefficient:

$$\dot{c}_L' = \frac{f_1}{T_P}\left(c_L^{\mathrm{c}} - c_L' \right) \tag{8}$$

with $f_1 = 2V/c$, where c is the chord length and V is the airspeed at 25% chord, and the dimensionless time constant T_P. For the state c_L' an equivalent angle of attack can be computed:

$$\alpha_f = c_L'/c_{L\alpha} \tag{9}$$

Moreover, for this delayed angle of attack α_f an equivalent separation point f'

$$f' = f^{\mathrm{st}}(\alpha_f) \tag{10}$$

can be computed. The second state f'' is the delayed flow separation point, again modeled with a first-order lag process:

$$\dot{f}'' = \frac{f_1}{T_f}\left(f' - f'' \right) \tag{11}$$

with the dimensionless time constant T_f .

Finally, the nonlinear airfoil coefficients can be calculated:

$$c_N = c_{L\alpha}\left(\frac{1+\sqrt{f''}}{2}\right)^2 \cos\alpha_E \tag{12}$$

$$c_D = \left(c_L^f - c_L^{\mathrm{st}}\right)\sin\alpha + c_D^{\mathrm{st}} \tag{13}$$

$$c_m = c_m^{\mathrm{st}} + (K_0 + K_1(1-f) + K_2\sin(\pi f^m)) \tag{14}$$

where the values of K_0, K_1, K_2 and m can be adjusted for different airfoils [19].

3. Spanwise wing downwash

When moving from 2D airfoil aerodynamics (Sections II.A.1 and II.A.2) to 3D wing aerodynamics, the induced velocity of the wing must be considered. For wings with moderate to high aspect ratio, the induced velocity in the wing depth direction can be neglected, so that only the induced velocity in the spanwise direction has to be considered. This means that it is sufficient to discretize the wing only in the spanwise direction.

The effective angle of attack of the local wing strips along the span, see Fig. 3, is manipulated by an induced angle of attack computed by a nonlinear steady lifting line theory [23] similar to [29, 30]. The method used is a VLM which has only one panel in the wing chord direction. This model provides a suitable spanwise lift distribution even for more complex wing geometries.

First, the associated circulation is calculated for all strips $i \in [1...L]$ along the span:

$$\Gamma_i = \frac{1}{2}V_{\infty,i}c_{L,i}^{\mathrm{c}}c_i \tag{15}$$

If the influence coefficients $\boldsymbol{A}_{\mathrm{ic}} \in \mathbb{R}^{L\times L}$ are known, the effective incident flow velocity in the normal direction for all strips

$$\boldsymbol{V}_n = \boldsymbol{A}_{\mathrm{ic}}\boldsymbol{\Gamma} \tag{16}$$

can be calculated, where $\boldsymbol{\Gamma} \in \mathbb{R}^L$ contains the local circulations Γ_i and $\boldsymbol{V}_n \in \mathbb{R}^L$ contains the local $V_{n,i}$. Since the inflow $V_{n,i}$ is known for each strip i, the effective angle of attack of the lifting line method can be calculated:

$$\alpha_{ll,i} = \arcsin\left(\frac{V_{n,i}}{V_{\infty,i}}\right) \tag{17}$$

The difference from the inflow angle of attack

$$\Delta\alpha_i = \alpha_{ll,i} - \alpha_{\infty,i} \tag{18}$$

can be attributed to viscous effects from the nonlinear lift coefficients. The corresponding expected lift coefficient from the nonlinear airfoil data

$$c_{L,\infty,i} = 2\pi(\alpha_{\infty,i} + \Delta\alpha_i) \tag{19}$$

is used to compute the necessary induced angle of attack of each strip

$$\bar{\alpha}_{\mathrm{ind},i} = \frac{c_{L,\infty,i} - c_{L,\mathrm{c},i}}{2\pi} \tag{20}$$

This induced angle of attack for each strip $\bar{\alpha}_{\mathrm{ind},i}$ is subtracted from the inflow angle of attack $\alpha_{\infty,i}$, see Fig. 4. This adjusts the angle of attack α_i of the unsteady airfoil model. To avoid iterations at each time step, the calculated induced angle of attack is filtered with a first-order low-pass filter:

$$\dot{\alpha}_{\mathrm{ind},i} = \frac{1}{T_{\mathrm{dw}}}\left(\bar{\alpha}_{\mathrm{ind},i} - \alpha_{\mathrm{ind},i}\right) \tag{21}$$

If the time constant T_{dw} is small enough, this method converges against the iterative solution, but has the advantages that the model is smooth and less computationally intensive.

4. Forces and Moments

The nonlinear airfoil coefficients $c_{L,i}$, $c_{D,i}$ and $c_{m,i}$ are converted to a force vector and pitching moment for the corresponding wing strip i. For both the force and the pitching moment, the coefficients have to be multiplied with the dynamic pressure $\rho/2 \cdot |\boldsymbol{V}_i|^2$ and the local span b_i and local chord c_i. The pitching moment simply is:

$$M_{A,i} = c_m \frac{\rho}{2} |\boldsymbol{V}_i|^2 b_i c_i^2 \tag{22}$$

The drag acts into the direction of the local inflow vector $\boldsymbol{V}_i$, while the lift coefficient acts perpendicular to the local inflow vector $\boldsymbol{V}_i$ and to the local vector in spanwise direction at the 25% chord line $\boldsymbol{\zeta}_i$. So, the wing strip force vector in body frame is:

$$\boldsymbol{R}_{Ab,i} = \frac{\rho}{2} |\boldsymbol{V}_i|^2 b_i c_i \left(\frac{\boldsymbol{V}_{b,i}}{|\boldsymbol{V}_{b,i}|} c_{D,i} + \frac{\boldsymbol{\zeta}_{b,i} \times \boldsymbol{V}_{b,i}}{|\boldsymbol{\zeta}_{b,i} \times \boldsymbol{V}_{b,i}|} c_{L,i} \right) \tag{23}$$

5. Tailplane

In the previous Sections II.A.3 and II.A.4, only the aerodynamics of a wing were described. To model the airplane aerodynamics, three wing models are combined, one for the main wing, one for the horizontal tailplane and one for the vertical tailplane. Furthermore, the downwash of the main wing, which has a delayed effect on the horizontal tailplane, is modeled according to [5].

B. Reduced-Order Structural Model

For the reduced-order structural model, a detailed FEM model is reduced to beam-element model, see Fig. 3, where the nodes are placed at the load reference axes, fuselage center line, and the engine positions. The linear beam-element model consisting of N nodes, each with three translational and three rotational degrees of freedom

$$\boldsymbol{M}\ddot{\boldsymbol{q}} + \boldsymbol{D}\dot{\boldsymbol{q}} + \boldsymbol{K}\boldsymbol{q} = \boldsymbol{f} \tag{24}$$

with mass matrix $\boldsymbol{M} \in \mathbb{R}^{6N \times 6N}$, stiffness matrix $\boldsymbol{K} \in \mathbb{R}^{6N \times 6N}$, damping matrix $\boldsymbol{D} \in \mathbb{R}^{6N \times 6N}$, load vector $\boldsymbol{f} \in \mathbb{R}^{6N}$ and displacement vector $\boldsymbol{q} \in \mathbb{R}^{6N}$, is then further reduced by applying the displacement method [31]:

$$\boldsymbol{M}_\mathrm{r}\ddot{\boldsymbol{\eta}} + \boldsymbol{D}_\mathrm{r}\dot{\boldsymbol{\eta}} + \boldsymbol{K}_\mathrm{r}\boldsymbol{\eta} = \boldsymbol{f}_\mathrm{r} \tag{25}$$

where the displacement vector $\boldsymbol{q}$ is replaced by K modal coordinates $\boldsymbol{\eta} \in \mathbb{R}^K$ with

$$\boldsymbol{M}_\mathrm{r} = \boldsymbol{\Phi}^T \boldsymbol{M} \boldsymbol{\Phi} \tag{26}$$

$$\boldsymbol{D}_\mathrm{r} = \boldsymbol{\Phi}^T \boldsymbol{D} \boldsymbol{\Phi} \tag{27}$$

$$\boldsymbol{K}_\mathrm{r} = \boldsymbol{\Phi}^T \boldsymbol{K} \boldsymbol{\Phi} \tag{28}$$

$$\boldsymbol{f}_\mathrm{r} = \boldsymbol{\Phi}^T \boldsymbol{f} \tag{29}$$

and

$$\left(\boldsymbol{K} - \omega_j^2 \boldsymbol{M} \right) \phi_j = \boldsymbol{0} \tag{30}$$

where ϕ_j is the mode shape vector corresponding to the eigenfrequency ω_j, with $j \in [1, ..., 6N]$

$$\boldsymbol{q} = \sum_{j=1}^{K} \phi_j \eta_j + \underbrace{\sum_{j_t=K+1}^{6N} \phi_{j_t} \eta_{j_t}}_{\text{truncated}} \tag{31}$$

C. Flexible-Body Equations of Motion

The flexible equations of motion are implemented according to Waszak & Schmidt [10], which are applicable for moderately flexible airplanes and computationally efficient. Thus, the rigid-body frame (index b) is the "practical" mean

axis system:

$$\dot{\boldsymbol{V}}_{Kb} = 1/m \left(\boldsymbol{R}_b + \boldsymbol{M}_{bg} \begin{bmatrix} 0 & 0 & g \end{bmatrix}^T - \boldsymbol{\Omega}_{Kb} \times \boldsymbol{V}_{Kb} \right) \tag{32}$$

$$\dot{\boldsymbol{\Omega}}_{Kb} = \boldsymbol{I}_b^{-1} \left(\boldsymbol{Q}_b - \boldsymbol{\Omega}_{Kb} \times (\boldsymbol{I}_b \boldsymbol{\Omega}_{Kb}) \right) \tag{33}$$

$$\ddot{\boldsymbol{\eta}} = \boldsymbol{M}_{\mathrm{r}}^{-1} \left(\boldsymbol{f}_{g,\mathrm{r}} + \boldsymbol{f}_{\mathrm{r}} - \boldsymbol{K}_{\mathrm{r}} \boldsymbol{\eta} - \boldsymbol{D}_{\mathrm{r}} \dot{\boldsymbol{\eta}} \right) \tag{34}$$

with the sum of all external forces in body frame $\boldsymbol{R}_b$, the sum of all external moments in body frame $\boldsymbol{Q}_b$, the rotation matrix from the inertial frame (index g) and the body frame $\boldsymbol{M}_{bg}$, the angular velocity vector of b w.r.t. g $\boldsymbol{\Omega}_K$, the velocity vector of b w.r.t. g V_K,the total mass m, the gravitational acceleration g, the total inertia matrix $\boldsymbol{I}$, and the generalized load vector in modal coordinates $\boldsymbol{f}_{\mathrm{r}}$. The vector of forces and moments due to gravity $\boldsymbol{f}_{\mathrm{g}}$ results from the mass of the nodes m_j, from the distances of the centers of mass from the nodes $\Delta \boldsymbol{r}_{b,cg,j}$ and from the attitude $\boldsymbol{M}_{bg}$:

$$\boldsymbol{f}_{\mathrm{g,r}} = \boldsymbol{\Phi}^T \boldsymbol{f}_g \tag{35}$$

$$\boldsymbol{f}_{g,j} = \begin{bmatrix} \boldsymbol{G}_{b,j} & \Delta \boldsymbol{r}_{b,cg,j} \times \boldsymbol{G}_{b,j} \end{bmatrix}^T \tag{36}$$

$$\boldsymbol{G}_{b,j} = m_j \boldsymbol{M}_{bg} \begin{bmatrix} 0 & 0 & g \end{bmatrix}^T \tag{37}$$

This model neglects all inertial coupling between the free vibrations model in Eq. (34) and the rigid body rotational motion in Eqs. (32) and (33). Moreover, the model neglects the effects of variable inertia. More accurate models would include all inertial coupling and varying inertia, which can be found in literature, e.g. [11]. However, there is the advantage that no iterations are necessary per time step to numerically solve a nonlinear system of equations.

D. Coupling of Aerodynamics Model and Flexible-Body Equations of Motion

In this section, the coupling of the aerodynamics model from Section II.A with the flexible-body equations of motion from Section II.C is presented. Figure 6 shows an overview of the coupling. The coupling is implemented such that no time consuming iterations are required at each time step. This is due to the fact that only states are included in the

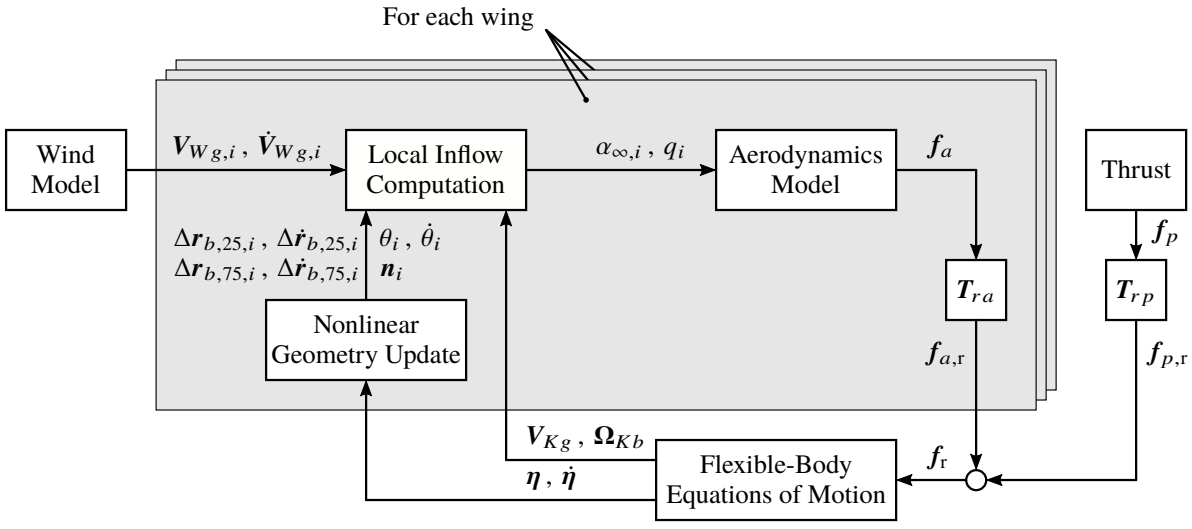

Fig. 6 Overview of Coupling of Aerodynamics and Structural Model.

feedback, namely $\boldsymbol{\eta}$, $\dot{\boldsymbol{\eta}}$, $\boldsymbol{V}_{Kg}$ and $\boldsymbol{\Omega}_{Kb}$. The coupling is performed in parallel for all wings, i.e. main wing, horizontal tailplane and vertical tailplane. The linear coupling via the matrix $\boldsymbol{T}_{ra}$ is discussed in Section II.D.1 In Section II.D.2 the nonlinear geometry update is presented. The nonlinear computation of the local inflow is presented in Section II.D.3. The thrust force is constant during all simulations performed in this work and is applied at the associated structural nodes.

1. Transformation matrix $\boldsymbol{T}_{ra}$

The constant transformation matrix $\boldsymbol{T}_{ra} \in \mathbb{R}^{K\times 4L}$, where K is the number of modal coordinates and L is the number of aerodynamic panels of the wing, is based on linear interpolation and is used to convert quantities from the aerodynamics coordinates to the structural coordinates.

For each structural node, it is checked whether it belongs to an aerodynamic panel. For this purpose, the aerodynamic panels are expanded to form a hexahedron so that it is easy to check whether a structural node lies within the hexahedron's volume. Thus, it is possible that a structural node does not belong to any aerodynamic panel or to one aerodynamic panel. Therefore, a Boolean matrix $\boldsymbol{T}_{\text{match}} \in \mathbb{R}^{M\times N}$ is introduced to map N total structural nodes to M matched structural nodes.

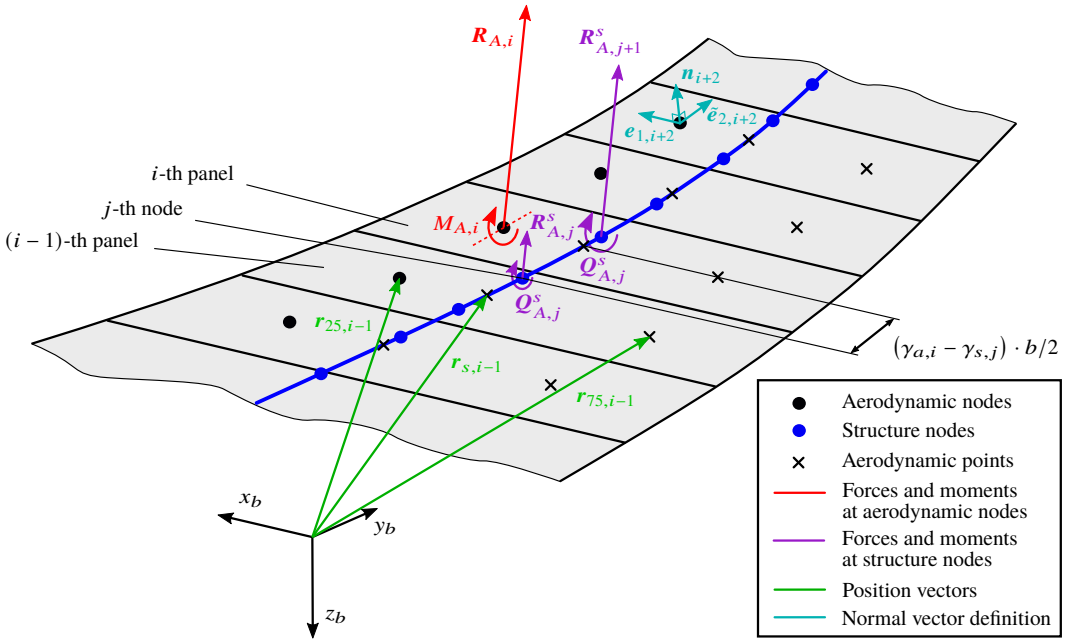

Fig. 7 Illustration of Coupling of Wing Aerodynamics and Structural Model.

The derivation of the transformation matrices is illustrated by Fig. 7. There are N structural nodes and L panels or strips for the wing aerodynamics model. At each panel there is an aerodynamic node at the 25% chord line $\boldsymbol{r}_{25,i}$ and two further aerodynamics points $\boldsymbol{r}_{75,i}$ at the 75% chord line and $\boldsymbol{r}_{s,i}$ at the intersection with the structure beam-element. The aerodynamic forces vector $\boldsymbol{R}_{A,i}$ and the pitching moment $M_{A,i}$ of each panel i are located at the aerodynamic node $\boldsymbol{r}_{25,i}$. The aerodynamic force and moment must be applied at the structural nodes such that the total force vector is equal and the total moment is equal with respect to a reference point. Therefore, the aerodynamic nodes and the structural dynamic nodes are given a dimensionless position $\boldsymbol{\gamma}_a$ in the spanwise direction with $-1 \le \boldsymbol{\gamma}_{a,i} \le 1$ for all $i \in [1...L]$ and $\boldsymbol{\gamma}_s$ with $-1 \le \boldsymbol{\gamma}_{s,j} \le 1$ for all $j \in [1...M]$, respectively. Then the nodes are sorted in spanwise direction:

$$\boldsymbol{\gamma}_{a,\text{sort}} = \boldsymbol{T}_{a,\text{sort}}\boldsymbol{\gamma}_a \tag{38}$$

$$\boldsymbol{\gamma}_{s,\text{sort}} = \boldsymbol{T}_{s,\text{sort}}\boldsymbol{\gamma}_s \tag{39}$$

with Boolean matrices $\boldsymbol{T}_{a,\text{sort}}$ and $\boldsymbol{T}_{s,\text{sort}}$ so that $\gamma_{a,\text{sort},i+1} > \gamma_{a,\text{sort},i}$ for all $i \in [1...L-1]$ and $\gamma_{s,\text{sort},i+j} > \gamma_{s,\text{sort},j}$ for all $j \in [1...M-1]$.

An interpolation matrix $\boldsymbol{T}_{sa,\text{sort},ij} \in \mathbb{R}^{M\times L}$ is introduced. For each aerodynamic node or for each point $\boldsymbol{r}_{s,i}$, the structural node to the left and to the right of it is determined. For the adjacent nodes, the matrix is filled so that the

division of the force vector into two force vectors produces the same moment:

$$T_{sa,\mathrm{sort},ji} = \begin{cases} \frac{\gamma_{s,j+1}-\gamma_{a,i}}{\gamma_{s,j+1}-\gamma_{s,j}} & \text{if } \gamma_{s,j+1} > \gamma_{a,i} > \gamma_{s,j} \\ 0 & \text{otherwise} \end{cases} \tag{40}$$

$$T_{sa,\mathrm{sort},j+1i} = \begin{cases} 1 - T_{sa,\mathrm{sort},ji} & \text{if } \gamma_{s,j+1} > \gamma_{a,i} > \gamma_{s,j} \\ 0 & \text{otherwise} \end{cases} \tag{41}$$

As an example, Fig. 7 shows how the red force is split into the two purple forces. The interpolation matrix for the unsorted node vectors is:

$$\tilde{\boldsymbol{T}}_{sa} = \boldsymbol{T}_{\mathrm{match}}^{T} \boldsymbol{T}_{s,\mathrm{sort}}^{T} \boldsymbol{T}_{sa,\mathrm{sort}} \boldsymbol{T}_{a,\mathrm{sort}} \tag{42}$$

The load vector per strip from the aerodynamics model

$$\boldsymbol{f}_{a,i} = \begin{bmatrix} \boldsymbol{R}_{Ab,i} \\ M_{A,i} \end{bmatrix} \tag{43}$$

has only four elements because only a one-dimensional pitching moment $M_{A,i}$ is modeled. The load vector per node from the structural dynamics model

$$\boldsymbol{f}_{s,j} = \begin{bmatrix} \boldsymbol{R}_{Ab,j}^{s} \\ \boldsymbol{Q}_{Ab,j}^{s} \end{bmatrix} \tag{44}$$

has six elements. A transformation matrix $\boldsymbol{T}_{sa} \in \mathbb{R}^{6N \times 4L}$ is introduced which transforms the load vector of the aerodynamic model into the load vector of the structural model:

$$\boldsymbol{f}_s = \boldsymbol{T}_{sa} \boldsymbol{f}_a \tag{45}$$

For this purpose, the submatrices of the transformation matrix are to be filled with the elements of the interpolation matrix $\tilde{\boldsymbol{T}}_{sa}$ as follows:

$$\boldsymbol{T}_{sa,ji} = \begin{bmatrix} \tilde{T}_{sa,ji} & 0 & 0 & 0 \\ 0 & \tilde{T}_{sa,ji} & 0 & 0 \\ 0 & 0 & \tilde{T}_{sa,ji} & 0 \\ 0 & 0 & 0 & 0 \\ 0 & 0 & -\left(x_{b,25,i} - x_{b,s,i}\right) \tilde{T}_{sa,ji} & \cos\left(\nu_i\right) \tilde{T}_{sa,ji} \\ 0 & \left(x_{b,25,i} - x_{b,s,i}\right) \tilde{T}_{sa,ji} & 0 & \sin\left(\nu_i\right) \tilde{T}_{sa,ji} \end{bmatrix} \tag{46}$$

Here, the lever arm $\left(x_{b,25,i} - x_{b,s,i}\right)$ and the dihedral angle

$$\nu_i = \arctan\left(\frac{z_{b,25,i+1} - z_{b,25,i-1}}{y_{b,25,i+1} - y_{b,25,i-1}}\right) \tag{47}$$

must be taken into account when calculating the moment vector. Finally, the transformation matrix $\boldsymbol{T}_{ra}$ is formed by multiplication with the mode shape matrix:

$$\boldsymbol{f}_{a,\mathrm{r}} = \boldsymbol{T}_{ra} \boldsymbol{f}_a = \boldsymbol{\Phi}^T \boldsymbol{T}_{sa} \boldsymbol{f}_a \tag{48}$$

2. Nonlinear Geometry Update

For the transformation of the structural node positions and angles

$$\boldsymbol{q}_j = \begin{bmatrix} \Delta x_{b,s,j} & \Delta y_{b,s,j} & \Delta z_{b,s,j} & \Delta\Phi_j & \Delta\Theta_j & \Delta\Psi_j \end{bmatrix}^T \tag{49}$$

to the position and angles of the aerodynamic nodes

$$\boldsymbol{p}_i = \begin{bmatrix} \Delta x_{b,25,i} & \Delta y_{b,25,i} & \Delta z_{b,25,i} & \Delta\theta_i \end{bmatrix}^T = \begin{bmatrix} \Delta \boldsymbol{r}_{b,25,i} & \Delta\theta_i \end{bmatrix}^T \tag{50}$$

the transposed transformation matrix for the load from Eq. (46) can be used:

$$\boldsymbol{p}_i = \boldsymbol{T}_{sa,ji}^T \boldsymbol{q}_j \tag{51}$$

with the local twist angle $\Delta\theta$ of the wing. From the aerodynamic node displacement in Eq. (50), the displacement of the points on the 75% chord line can be calculated as a function of the local twist:

$$\Delta\boldsymbol{r}_{b,75,i} = \Delta\boldsymbol{r}_{b,25,i} + \begin{bmatrix} 0 & \left(x_{b,75,i} - x_{b,s,i}\right) \cdot \sin\nu_i & -\left(x_{b,75,i} - x_{b,s,i}\right) \cdot \cos\nu_i \end{bmatrix}^T \cdot \theta_i \tag{52}$$

Finally, the normal vector of the aerodynamic panels

$$\boldsymbol{n}_i = \tilde{\boldsymbol{n}}_i / |\tilde{\boldsymbol{n}}_i| \tag{53}$$

is calculated nonlinearly. For this purpose, the cross product of two vectors $\boldsymbol{e}_{1,i}$, $\tilde{\boldsymbol{e}}_{2,i}$ lying in the plane of the panel is used, as illustrated at the $(i+2)$-th panel in Fig. 7:

$$\tilde{\boldsymbol{n}}_i = \tilde{\boldsymbol{e}}_{2,i} \times \boldsymbol{e}_{1,i} \tag{54}$$

with

$$\boldsymbol{e}_{b,1,i} = \boldsymbol{M}(\nu_i\,,\,\theta_i) \begin{bmatrix} 1 \\ 0 \\ 0 \end{bmatrix}_b \quad \text{with} \quad \boldsymbol{M}(\nu_i\,,\,\theta_i) \begin{bmatrix} 1 & 0 & 0 \\ 0 & \cos\nu_i & -\sin\nu_i \\ 0 & \sin\nu_i & \cos\nu_i \end{bmatrix} \begin{bmatrix} \cos\theta_i & 0 & \sin\theta_i \\ 0 & 1 & 0 \\ -\sin\theta_i & 0 & \cos\theta_i \end{bmatrix} \tag{55}$$

$$\boldsymbol{e}_{b,2,i} = \boldsymbol{M}(\nu_i\,,\,\theta_i) \begin{bmatrix} 0 & 1 & 0 \end{bmatrix}_b^T \tag{56}$$

$$\tilde{\boldsymbol{e}}_{b,2,i} = \boldsymbol{e}_{b,2,i} + \begin{bmatrix} -\sin\varphi_i & 0 & 0 \end{bmatrix}^T \tag{57}$$

This requires the local twist angle

$$\theta_i = \theta_{0,i} + \Delta\theta_i \tag{58}$$

with the twist angle of the jig shape $\theta_{0,i}$ as well as the local wing sweep angle

$$\varphi_i = \arctan\left(\frac{x_{25,i+1} - x_{25,i-1}}{\sqrt{\left(y_{25,i+1} - y_{25,i-1}\right)^2 + \left(z_{25,i+1} - z_{25,i-1}\right)^2}} \right) \tag{59}$$

3. Local Inflow

The inflow vector at the points on the 75% chord line

$$\boldsymbol{V}_{Ab,75,i} = \boldsymbol{V}_{Kb} + \boldsymbol{\Omega}_{Kb} \times \boldsymbol{r}_{b,75,i} + \dot{\boldsymbol{r}}_{b,75,i} + \boldsymbol{V}_{Wb,i} \tag{60}$$

is composed of the kinematic velocity of the center of gravity $\boldsymbol{V}_{Kb}$, the fraction due to rotation of the center of gravity $\boldsymbol{\Omega}_{Kb} \times \boldsymbol{r}_{b,75,i}$, the fraction from the velocity due to structural deformation $\dot{\boldsymbol{r}}_{b,75,i}$, and the local wind vector $\boldsymbol{V}_{Wb,i} = \boldsymbol{M}_{bg}\boldsymbol{V}_{Wg,i}$ with the delayed local wind vector $\boldsymbol{V}_{Wg,i}$. For the inflow vector at the points of the 25% chord line

$$\boldsymbol{V}_{Ab,25,i} = \boldsymbol{V}_{Kb} + \boldsymbol{\Omega}_{Kb} \times \boldsymbol{r}_{b,25,i} + \dot{\boldsymbol{r}}_{b,25,i} + \boldsymbol{V}_{Wb,i} + \dot{\boldsymbol{V}}_{Wb,i} |\boldsymbol{r}_{b,25,i} - \boldsymbol{r}_{b,75,i}| / |\boldsymbol{V}_{Ab,75,i}| \tag{61}$$

an additional term for the wind gradient $\dot{\boldsymbol{V}}_{Wb,i} |\boldsymbol{r}_{b,25,i} - \boldsymbol{r}_{b,75,i}| / |\boldsymbol{V}_{Ab,75,i}|$ must be considered. The angle of attack at the points on the 25% chord line and the 75% chord line can be calculated from the incident flow component in the direction of the local normal vector:

$$\alpha_{\infty,25,i} = \arcsin\left(\left(\boldsymbol{V}_{A,25,i} \cdot \boldsymbol{n}_i\right) / |\boldsymbol{V}_{A,25,i}| \right) \tag{62}$$

$$\alpha_{\infty,75,i} = \arcsin\left(\left(\boldsymbol{V}_{A,75,i} \cdot \boldsymbol{n}_i\right) / |\boldsymbol{V}_{A,75,i}| \right) \tag{63}$$

The angle of attack for the airfoil aerodynamics model, see Fig. 6 and Fig. 4, is the angle of attack at the 25% point [28]:

$$\alpha_{\infty,i} = \alpha_{\infty,25,i} \tag{64}$$

The dimensionless pitch rate for the airfoil aerodynamics model, see Fig. 6 and Fig. 4, can be calculated from the difference of the angles of attack at the 75% chord point and at the 25% chord point [28]:

$$q_i = 2 \cdot \left(\alpha_{\infty,75,i} - \alpha_{\infty,25,i}\right) \tag{65}$$

E. Trimming and Linearization

To allow the aeroelastic model to be employed effectively, it must be possible to trim the aircraft, i.e. find the initial state and inputs of the system such that a simulation can be initialized at an equilibrium point. In this model, a root-finding approach is used. The trim function is allowed to vary a set of trim variables, i.e. a subset of the system's inputs and states, with the objective of reaching a set of trim requirements, i.e. desired output and state derivative values. The root-finding approach requires the number of trim variables and trim requirements to be equal. To reduce the complexity of the problem and avoid numerical issues, only steady aerodynamics are considered during trim; the initial values for the missing unsteady aerodynamic model states are derived from the steady aerodynamic model states after the successful completion of the trim computation.

For instance, to trim the aircraft in steady level flight (the most common scenario), the trim function aims for a specified altitude(which can be directly specified in the initial states) and airspeed. Its trim requirements therefore include the airspeed as output, as well as minimizing the state derivatives for altitude, vertical and longitudinal speed, pitch rate, and generalized rates ($\dot{\boldsymbol{\eta}}$ from Eq. 25). Trim variables include the HTP deflection, thrust, pitch angle, vertical and longitudinal inertial speeds, and generalized coordinates ($\boldsymbol{\eta}$).

The aircraft can furthermore be linearized around the trim point by numerically computing its Jacobian. This functionality is key for linear analysis (e.g. aeroelastic stability) and control design.

III. Application to Energy-Efficient Airplane

The reduced-order aeroelastic flight dynamics model presented in Section II is parameterized corresponding to the energy-efficient passenger airplane presented in Section I.

In Section III.A we briefly present the simulation model parameters and then show a validation of the aerodynamics model in Section III.B. Section III.C shows the gust load envelope and maximum occurring loads depending on the operating point, which were determined by numerous simulations.

A. Parametrization

The basic data of the energy-efficient airplane have already been mentioned in the introduction I. There and in Section II.B, it was also described how the structural model was created. The reduced-order beam element model consists of $N = 134$ nodes, of which $M = 60$ nodes were assigned to the main wing, $M = 16$ nodes to the horizontal tailplane, and $M = 10$ nodes to the vertical tailplane. The geometry for the aerodynamic model was automatically read from the CPACS file [32]. The wing is based on the DLR-F15 airfoil, for which the lift curves from Fig. 5 are used.

For the reduced-order structural dynamics model, see Section II.B, we used $K = 30$ mode shapes. A coupling of the first symmetrical bending mode (first mode, Fig. 14a) and first symmetrical torsion mode with engine tilting (third mode, Fig. 14b) tends to become marginally stable at high EAS. The symmetrical torsional mode is particularly vulnerable in this aircraft configuration due to the destabilizing influence of the over-wing engines. Based on level of structural damping allowed under CS-25 AMC25.629 (Aeroelastic Stability Requirements) [1], a structural modal damping of 1% is added to the first mode and a damping of 3% for the third mode. The remaining entries in the damping matrix $\boldsymbol{D}_\mathrm{r}$ are zero. The wing is divided into $L = 40$ panels, the horizontal tailplane into $L = 16$ panels, and the vertical tailplane into $L = 8$ panels. A time step size of 1/900 seconds and a Runge-Kutta solver are chosen. These discretization parameters represent a good compromise between accuracy and computation time. The mass distribution of the configurations considered is shown in Appendix IV.A. Also shown in Appendix IV.B are the first four symmetric eigenmodes.

B. Validation of the Aerodynamic Model

1. Description of the High-Fidelity Aerodynamic Model

Time-resolved flow simulations were conducted for the mid-range 3D aircraft configuration encountering a vertical gust. For this validation case, the aircraft was not allowed to pitch or plunge and the structure was considered as rigid. The simulated geometry was a simplified half-model without stabilizers or jet engines and the focus of the simulations was on evaluating the gust-induced wing load changes over time. The RANS equations were solved using the DLR-TAU code on a hybrid grid. The employed grid features 5.04 million points, 11.1 million cells, and was the result of a separately conducted study to guarantee independence of the solution from the grid resolution. The grid was created with a non-dimensional first layer thickness $y^+ \leq 0.5$ for a flight altitude of 6000 m with flight Mach number $M = 0.76$. Turbulence was modelled using the 1-equation Spalart-Allmaras formulation with Rotation and Curvature

Correction (SARC), which is a computationally inexpensive model suitable for external aerodynamic applications with a modification to better capture streamline curvature, as expected at the wing-fuselage junction of the geometry. The time integration was carried out using backward Euler method, while spatial discretization was conducted using 2nd order central scheme with scalar dissipation. The selected timestep size was $2 \cdot 10^{-4}$ s and a sufficiently high number of inner iterations per timestep was selected to converge the aerodynamic forces to a tolerance of 10^{-5}. The effect of timestep size on the solution was evaluated in a separate study and the largest possible timestep was selected that did not compromise the solution's accuracy. A vertical gust of 1–cos shape was simulated using the disturbance velocity approach (DVA) [33], which was previously shown to yield reliable results for the simulated gust length.

2. Comparison of the Aerodynamic Models

In this section the reduced-order aerodynamic model of Section II is compared with the high-fidelity model of Section III.B.1. Figure 8 shows a 1–cosine gust simulation of the airplane.

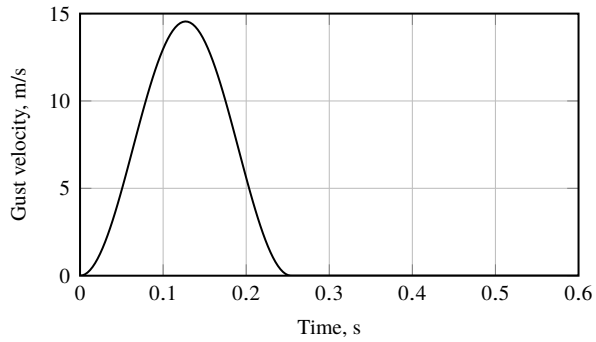

(a) Upward gust velocity at wing root front.

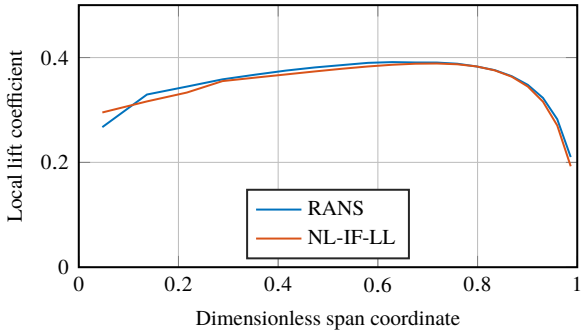

(b) Steady lift distribution without gust.

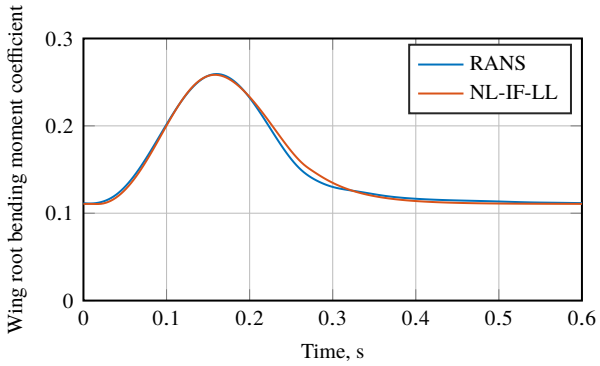

(c) Wing root bending moment coefficient response.

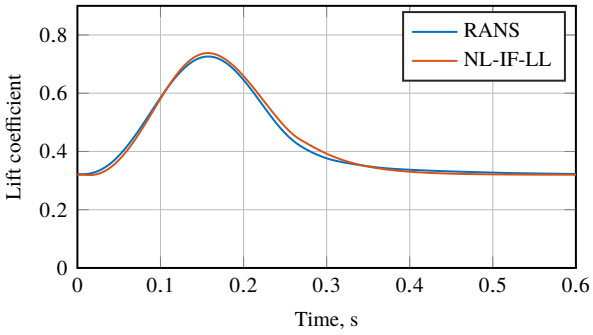

(d) Lift coefficient response.

Fig. 8 Comparison of NL-IF-LL and URANS for one gust: $H = 6000$ m, $M = 0.76$. The aircraft is not allowed to pitch or plunge and the structure is rigid.

It can be seen that the steady-state spanwise lift coefficient distribution is in good agreement. Smaller deviations exist in the area of the fuselage, because the fuselage influence is difficult to model accurately with potential-theoretical methods. The total lift coefficient agrees well during the gust interaction. There are minor deviations during the decay of the lift. The good agreement of the coefficient for the wing root bending moment shows that the spanwise lift distribution also agrees well during the gust interaction.

C. Open-Loop Gust Loads of the Energy-Efficient Airplane

Seeing as one of the main objectives of this model is to enable the design and evaluation of GLA functions, its gust load envelopes are computed and presented here as a demonstration of its capabilities. It was found in the course of these investigations that the trimmed flight shape of the flexible aircraft did not have the correct lift distribution. Consequently, the results shown below should not be considered definitive or representative of the aircraft design. Pending a redesign

of the twist angles of the wing jig shape, they should rather be interpreted as indicative of the general characteristics of the aircraft and the overall model.

In the present work, the open-loop gust load envelope is computed across the flight envelope based only on CS25.341(a) / FAR Part 25 §341(a) [1, 2], i.e. considering only symmetrical 1–cos discrete gusts. Eight gust half-lengths ranging from 9 m to 107 m are considered, and based on the values listed in Table 1, the vertical gust speeds can be computed as defined in the certification specifications. Gust interaction is modeled by defining the (one-dimensional) gusts in space and computing the local wind velocity for each aerodynamic panel based on its absolute position.

The flight envelope is defined by a grid of 80 flight points covering all speeds from V_{s1g} to V_D and from ground level to the maximum operating altitude. This results in slightly more than 2,500 gust encounters for each aircraft configuration. The structural loads are computed as cut loads from the generalized coordinates following the techniques in [11].

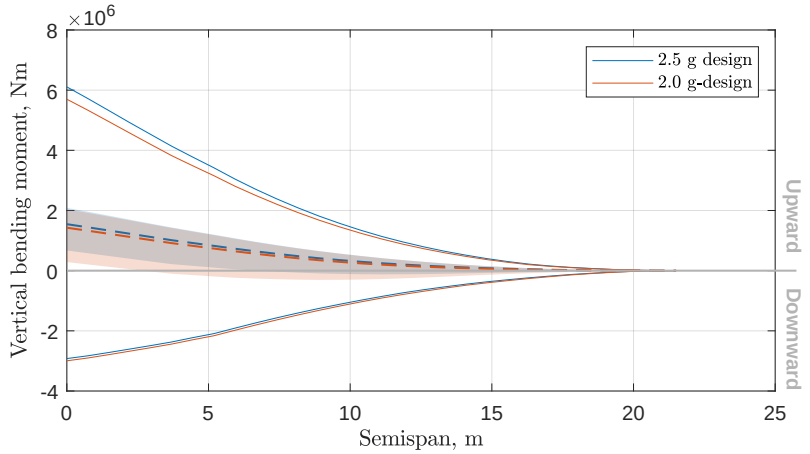

Fig. 9 Comparison of the vertical wing bending moment discrete gust load envelopes for the 2.5 g- and 2.0 g-designs. The dashed lines represent average trim loads, the shaded areas the range of trim loads, and the solid lines the limit gust loads. Other load types are shown in Appendix IV.D (Fig. 16)

Figure 9 shows the resulting wing vertical bending moment envelopes of the 2.5 g and 2.0 g airframes. Load envelopes of the remaining relevant loads, including the vertical bending moment, torsional moment, and vertical shear loads for the main wing and HTP, as well as the vertical bending moment and vertical shear loads for the fuselage, can be found in Appendix IV.D. In the case of the fuselage, the area corresponding to the wing box is excluded, as the structural model used here is considered too simple to adequately represent the loads in this section.

It is clear that the difference in peak loads between the two aircraft structures is minimal. The differences seen here can be mainly explained by the difference in trim loads: the heavier structure of the 2.5 g aircraft tends to generate higher trim loads, while the more-flexible 2.0 g airframe does not appear to experience significantly higher incremental loads.

To demonstrate the variations of the peak loads across the flight envelope, Fig. 10 shows the maximum and minimum peak wing root bending moment (WRBM) for both mass cases of the 2.5 g design. Each circle represents an evaluated operating point, the magnitude of the peak load is indicated by the color bar, and contour lines are added to help visualize the gradient over the flight envelope; note that the scale of the color bar is not consistent between figures. As expected, gust loads increase with increasing airspeed, and in all cases, the critical flight point corresponds to V_C at an altitude of 6000 m. The decrease in loads at speeds above V_C/M_C is caused by the reduction in gust speed between V_C and V_D defined in the certification specifications.

Figure 11 illustrates the differences between the 2.0 g and 2.5 g airframes more closely by examining the absolute difference in peak WRBM for the MTOW mass case only. As Fig. 9 already suggested, both the upward and downward peak bending moments are generally lower in the 2.0 g aircraft. The biggest differences occur at higher speeds and at mid-to-low altitudes, implying that the 2.0 g structure is somewhat more sensitive to gust loads at high altitudes.

Figure 12 instead examines the effect of the stall model on loads for the MTOW mass case of the 2.5 g aircraft. It is shown in [15, 21, 22] that stall may have an important effect on the peak gust loads by reducing the peak aerodynamic loads. Indeed, Fig. 5 shows that the stall angle of attack and the maximum lift coefficient tend to decrease with increasing Mach number, potentially strengthening this effect at the higher speeds which are typically sizing for gust loads.

In the results presented here, the most significant differences in WRBM are visible at low speeds for upward-directed gust loads. In that part of the flight envelope, the aircraft is already flying at a high angle of attack/lift coefficient, so an upward gust quickly stalls the wing. Though not shown here, the OEW case has far smaller differences due to its lower mass and therefore lower stalling speed. A small part of the flight envelope, centered around the flight point 11,200 m and Mach 0.77 (Fig. 12b) does demonstrate a significant reduction in bending loads thanks to stall effects. This effect is due to the fact that at this operating point a relatively high angle of attack is achieved at a relatively high Mach number, which favors stall in the airfoil used, see Fig. 5. Overall, however, the gust load envelopes are mostly unaffected by the stall model because the sizing cases all occur in the higher-speed medium-altitude portion of the envelope, as suggested already by Fig. 10, and the same can be said for the 2.0 g aircraft.

The lack of an effect at higher speeds can be justified by two important aspects. Firstly, in[15, 21, 22], the lift coefficients at the considered design point are higher than those of the present aircraft's design point, such that there is overall less margin to stall. Secondly, these studies all considered fixed, rigid structures, whereas the aircraft model shown here is flexible and free to move in the vertical plane. Locally, the pitching and heaving motions of the airfoil sections tend to delay or even avoid an aerodynamic stall, thus minimizing the impact on loads. It is therefore conceivable that stall could have a greater impact on peak loads for a heavier (i.e. with higher wing loading), more rigid aircraft, however, in the current case they do not affect the sizing loads.

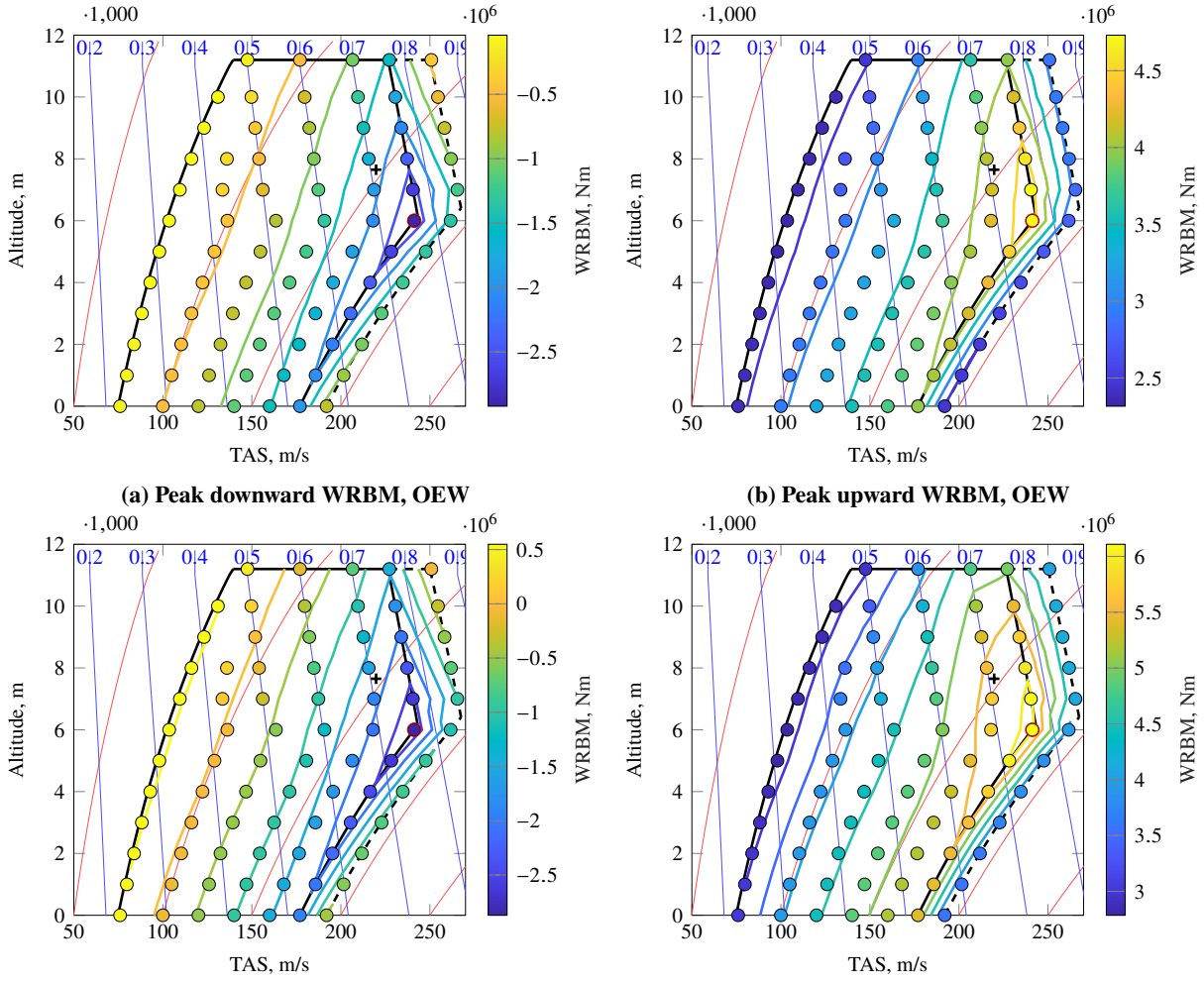

(a) Peak downward WRBM, OEW

(b) Peak upward WRBM, OEW

(c) Peak downward WRBM, MTOW

(d) Peak upward WRBM, MTOW

Fig. 10 Peak maximum/minimum wing root bending moment of the 2.5 g design across the flight envelope and for both mass cases. The red circle indicates the flight point with the greatest absolute value.

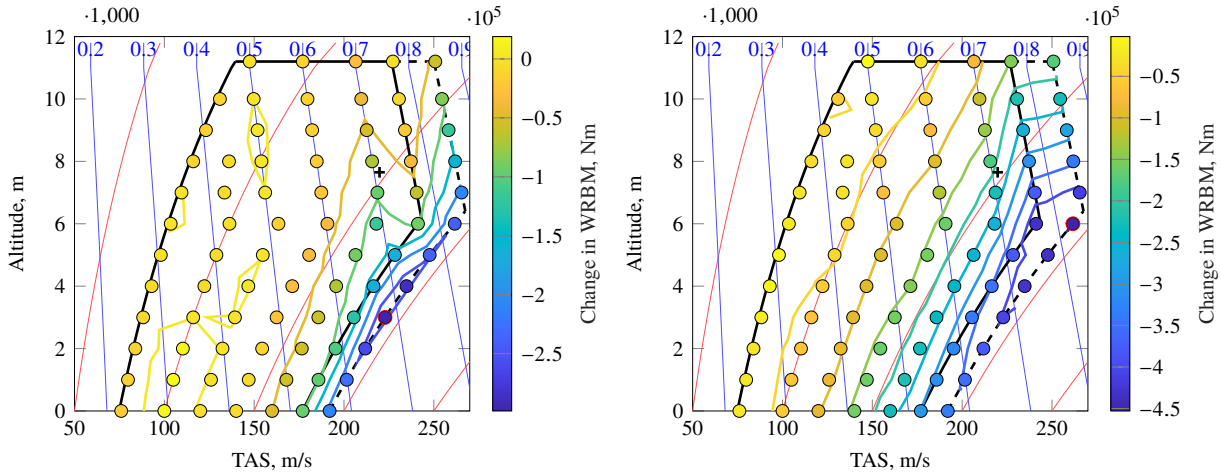

(a) Difference in peak downward WRBM, MTOW **(b) Difference in peak upward WRBM, MTOW**

Fig. 11 Absolute difference in peak WRBM between the 2.0 g and 2.5 g designs.

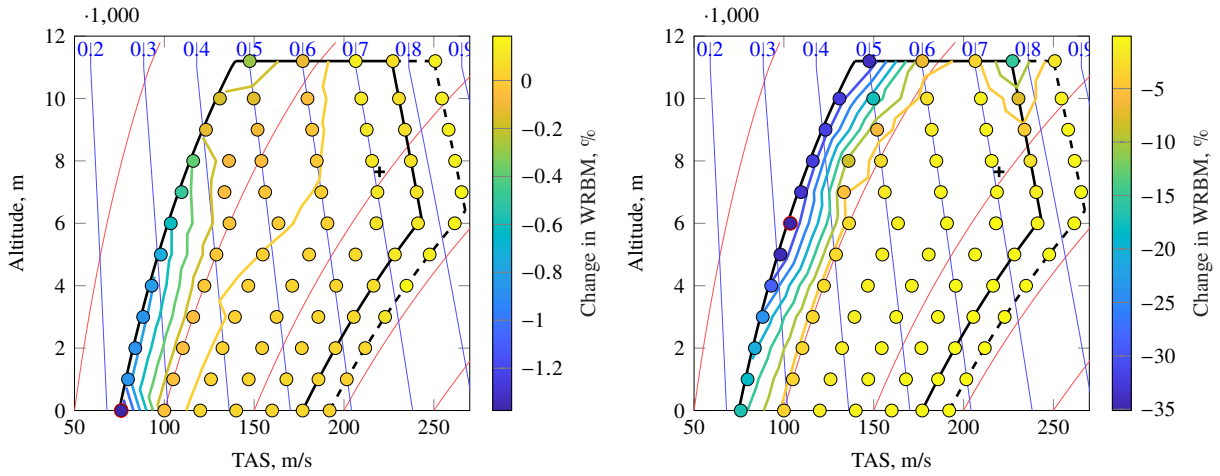

(a) Difference in peak downward WRBM, MTOW **(b) Difference in peak upward WRBM, MTOW**

Fig. 12 Relative impact of the stall model on peak WRBM for the 2.5 g design.

IV. Conclusions

In this paper we present a new and open-source aeroelastic flight dynamics model implemented in Matlab/Simulink. The unsteady aerodynamics model shows good agreement with URANS simulations and can also represent the effects of dynamic stall. This capability enables the design and evaluation of novel active load alleviation systems in the future.

The created model is parameterized corresponding to a novel energy-efficient passenger airplane designed for reduced loads. Through an automated workflow producing several thousand simulations, the gust load envelopes are calculated and the sizing operating points are identified. It is shown that the open-loop loads of the aircraft designed for reduced maneuver loads are approximately the same as those of the aircraft without reduced loads. It is also shown that dynamic stall mostly occurs at low airspeeds, whereas maximum loads occur at high speeds. Thus, for the aircraft under investigation, there is no reduction in peak gust loads due to stall.

In the immediate future, a redesign of the wing twist angles will be performed to correct the flexible aircraft's lift distribution in flight and produce the correct loads. Future investigations could examine whether dynamic stall can be further encouraged at high airspeeds to passively reduce gust loads, e.g. by increasing the lift coefficient at the design point. Furthermore, the gust loads and aerodynamic behavior of rigid and elastic structures could be compared to help bridge the gap between (typically rigid) high-fidelity aerodynamic simulations and lower-fidelity aeroelastic simulations.

Acknowledgments

We would like to acknowledge the funding by the Deutsche Forschungsgemeinschaft (DFG, German Research Foundation) under Germany's Excellence Strategy – EXC 2163/1 - Sustainable and Energy Efficient Aviation – Project-ID 390881007.

Appendix

A. Mass Distributions

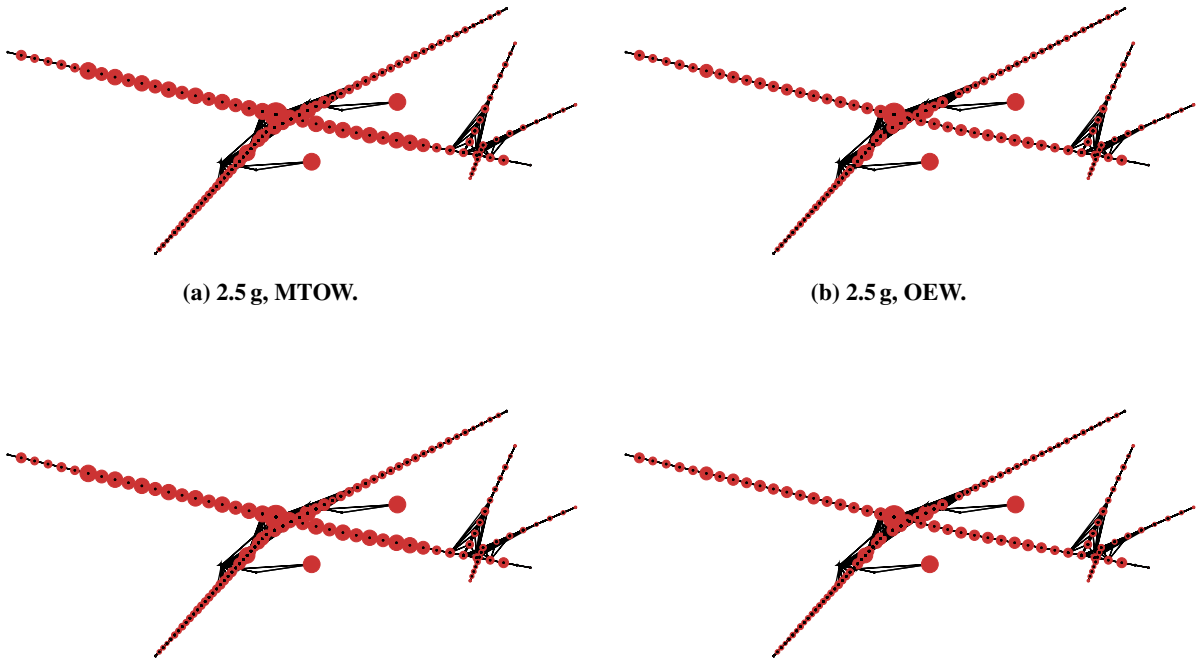

(a) 2.5 g, MTOW. **(b) 2.5 g, OEW.**

(c) 2.0 g, MTOW. **(d) 2.0 g, OEW.**

Fig. 13 Mass distributions of the 2.5 g and 2.0 g configurations.

B. Eigenmodes

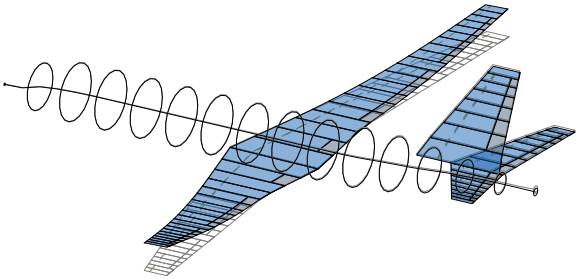

(a) 1st mode, frequency: 9.84 rad/s.

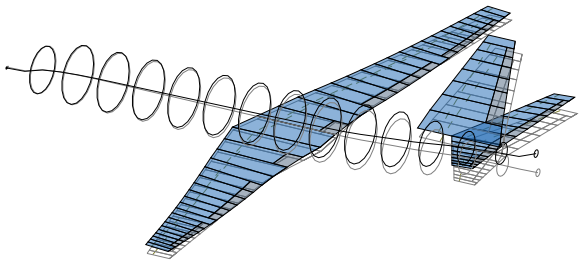

(b) 3rd mode, frequency: 17.5 rad/s.

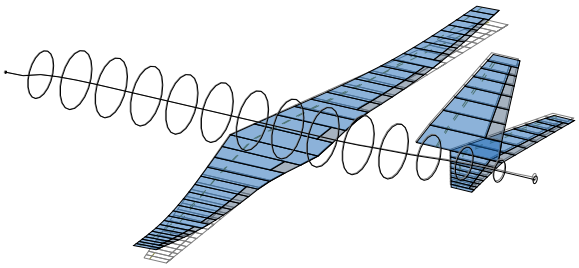

(c) 5th mode, frequency: 24.2 rad/s.

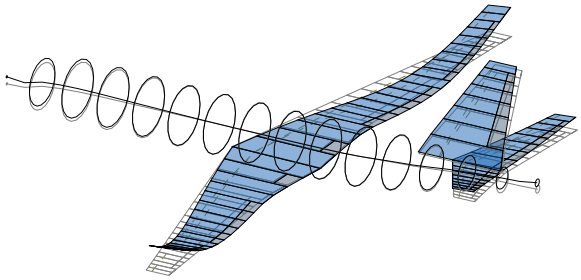

(d) 7th mode, frequency: 29.8 rad/s.

Fig. 14 Eigenmodes of 2.0 g configuration with MTOW.

C. Illustration of a Single Gust Simulation

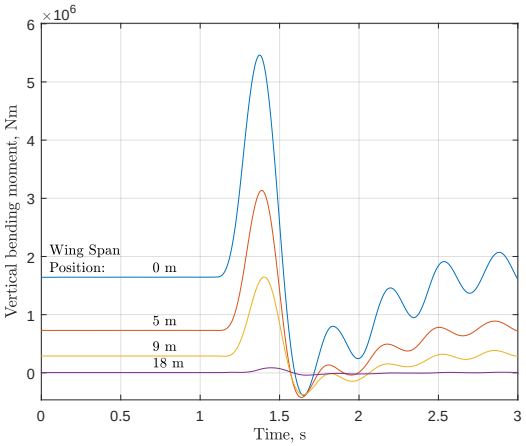

(a) Vertical bending moment at selected points along the wing.

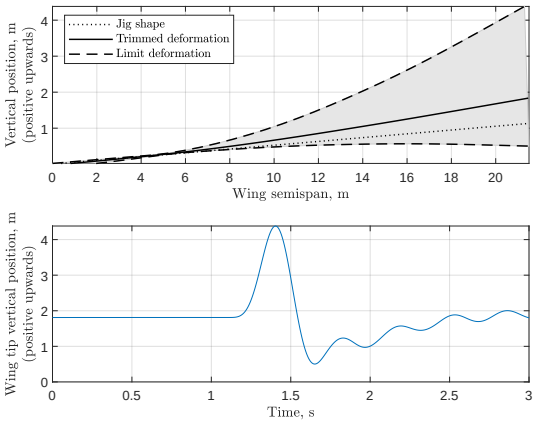

(b) Wing structure deformation.

Fig. 15 Illustration of a single gust encounter for the 2.5 g aircraft: 1–cos upward gust with 45 m gust gradient starting approximately after 1 second. The aircraft starts in trimmed level flight at 240 m/s true airspeed/Mach 0.77 and 6000 m altitude.

D. Comparison of Gust Load Envelopes

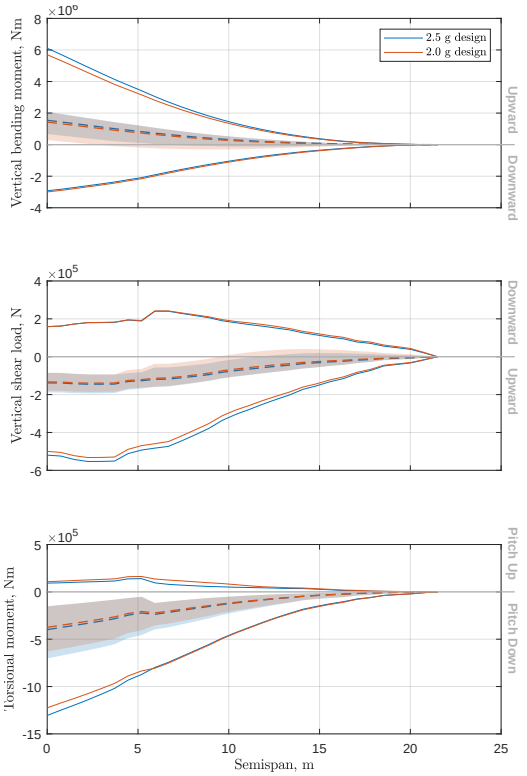

(a) Wing loads

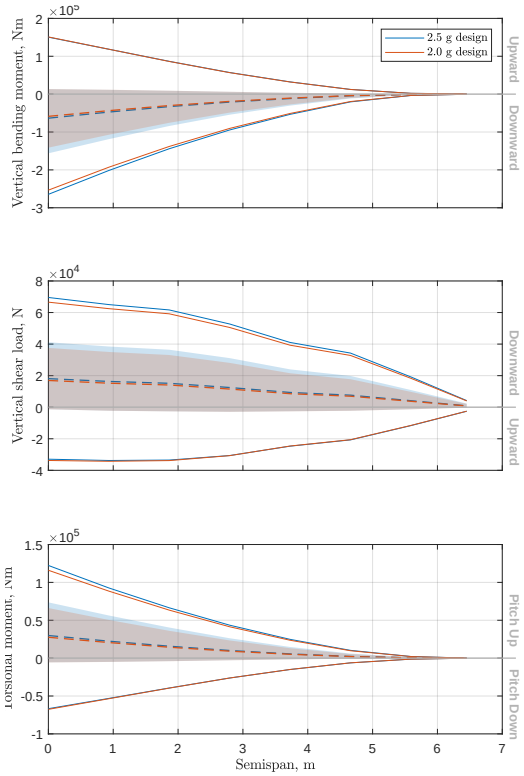

(b) HTP loads

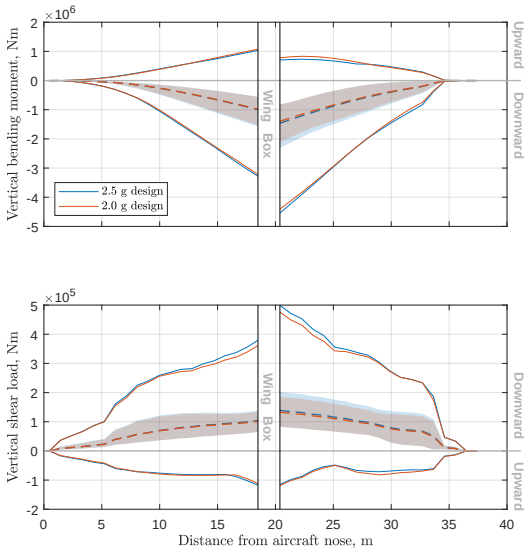

(c) Fuselage loads

Fig. 16 Comparison of the discrete gust load envelopes of the 2.5 g- and 2.0 g-designs. The dashed lines represent average trim loads, the shaded areas the range of trim loads, and the solid lines the limit gust loads.

References

[1] EASA, *CS-25: Certification Specifications and Acceptable Means of Compliance for Large Aeroplanes*, Vol. Amendment 27, European Union Aviation Safety Agency, 2023.

[2] "CFR Title 14 Vol 1 Part 25 - Airworthiness Standards: Transport Category Airplanes," , 2020.

[3] Allison, R. L., Perkin, B. R., and Schoenman, R. L., "Application of Winglets and/or Wing Tip Extensions with Active Load Control on the Boeing 747," *CTOL Transport Technology 1978*, NASA Langley Research Center, Hampton, Virginia, 1978.

[4] Dussart, G., Portapas, V., Pontillo, A., and Lone, M., "Flight dynamic modelling and simulation of large flexible aircraft," *Flight physics–models, techniques and technologies*, IntechOpen, London, UK, 2018. https://doi.org/10.5772/intechopen.71050.

[5] Andrews, S. P., "Modelling and simulation of flexible aircraft: handling qualities with active load control," Ph.D. thesis, School of Engineering, Cranfield Univ., Cranfield, England, U.K., 2011.

[6] Portapas, V., Cooke, A., and Lone, M., "Modelling framework for flight dynamics of flexible aircraft," *Aviation*, Vol. 20, No. 4, 2016, pp. 173–182. https://doi.org/10.3846/16487788.2016.1264719.

[7] Ritter, M., Teixeira, P., and Cesnik, C. E., "Comparison of nonlinear aeroelastic methods for maneuver simulation of very flexible aircraft," *2018 AIAA/ASCE/AHS/ASC Structures, Structural Dynamics, and Materials Conference*, Kissimmee, Florida, USA, 2018. https://doi.org/10.2514/6.2018-1953.

[8] Su, W., "Coupled Nonlinear Aeroelasticity and Flight Dynamics of Fully Flexible Aircraft," Ph.D. thesis, Univ. of Michigan, Ann Arbor, MI, USA, 2008.

[9] Pang, Z. Y., "Modeling, Simulation and Control of Very Flexible Unmanned Aerial Vehicle," Ph.D. thesis, Univ. of Michigan, Ann Arbor, MI, USA, 2018.

[10] Waszak, M. R., and Schmidt, D. K., "Flight dynamics of aeroelastic vehicles," *Journal of Aircraft*, Vol. 25, No. 6, 1988, pp. 563–571. https://doi.org/10.2514/3.45623.

[11] Reschke, C., "Integrated flight loads modelling and analysis for flexible transport aircraft," Ph.D. thesis, University of Stuttgart, 2006.

[12] Shearer, C. M., and Cesnik, C. E., "Nonlinear flight dynamics of very flexible aircraft," *Journal of Aircraft*, Vol. 44, No. 5, 2007, pp. 1528–1545. https://doi.org/10.2514/1.27606.

[13] DeLaurier, J. D., "An aerodynamic model for flapping-wing flight," *The Aeronautical Journal*, Vol. 97, No. 964, 1993, pp. 125–130. https://doi.org/10.1017/S0001924000026002.

[14] Kier, T., "Comparison of unsteady aerodynamic modelling methodologies with respect to flight loads analysis," *AIAA Atmospheric Flight Mechanics Conference and Exhibit*, 2005. https://doi.org/10.2514/6.2005-6027.

[15] Ullah, J., Lutz, T., Klug, L., Radespiel, R., Wild, J., and Heinrich, R., "Approach for Aerodynamic Gust Load Alleviation by Means of Spanwise-Segmented Flaps," *Journal of Aircraft*, 2023, pp. 1–22. https://doi.org/10.2514/1.C037086.

[16] Kim, D.-K., Lee, J.-S., Lee, J.-Y., and Han, J.-H., "An aeroelastic analysis of a flexible flapping wing using modified strip theory," *Active and Passive Smart Structures and Integrated Systems 2008*, Vol. 6928, SPIE, 2008, pp. 477–484. https://doi.org/10.1117/12.776137.

[17] Silvestre, F. J., and Luckner, R., "Experimental validation of a flight simulation model for slightly flexible aircraft," *AIAA Journal*, Vol. 53, No. 12, 2015, pp. 3620–3636. https://doi.org/10.2514/1.J054023.

[18] Wang, X., Van Kampen, E., Chu, Q., and De Breuker, R., "Flexible aircraft gust load alleviation with incremental nonlinear dynamic inversion," *Journal of Guidance, Control, and Dynamics*, Vol. 42, No. 7, 2019, pp. 1519–1536. https://doi.org/10.2514/1.G003980.

[19] Leishman, J. G., and Beddoes, T., "A Semi-Empirical model for dynamic stall," *Journal of the American Helicopter Society*, Vol. 34, No. 3, 1989, pp. 3–17. https://doi.org/10.4050/JAHS.34.3.3.

[20] Hansen, M. H., Gaunaa, M., and Madsen, H. A., *A Beddoes-Leishman type dynamic stall model in state-space and indicial formulations*, Risø-R-1354(EN), Risø National Laboratory, Roskilde, Denmark, 2004.

[21] Asaro, S., Khalil, K., and Bauknecht, A., "Unsteady characterization of fluidic flow control devices for gust load alleviation," *New Results in Numerical and Experimental Fluid Mechanics XIII: Contributions to the 22nd STAB/DGLR Symposium*, Springer, 2021, pp. 153–163. https://doi.org/10.1007/978-3-030-79561-0_15.

[22] Khalil, K., Asaro, S., and Bauknecht, A., "Active flow control devices for wing load alleviation," *Journal of Aircraft*, Vol. 59, No. 2, 2022, pp. 458–473. https://doi.org/10.2514/1.C036426.

[23] Beyer, Y., Ullah, J., and Steen, M., "Unsteady Nonlinear Lifting Line Model for Active Gust Load Alleviation of Airplanes," [Unpublished manuscript], 2023. Institute of Flight Guidance, Technische Universität Braunschweig.

[24] Karpuk, S., Radespiel, R., and Elham, A., "Assessment of future airframe and propulsion technologies on sustainability of next-generation mid-range aircraft," *Aerospace*, Vol. 9, No. 5, 2022, p. 279. https://doi.org/10.3390/aerospace9050279.

[25] Klimmek, T., Schulze, M., Abu-Zurayk, M., Ilic, C., and Merle, A., "cpacs-MONA–An independent and in high fidelity based MDO tasks integrated process for the structural and aeroelastic design for aircraft configurations," *Proceedings of Forum of Aeroelasticity and Structural Dynamics IFASD 2019*, Savannah, GA, USA, 2019.

[26] Handojo, V., "Contribution to Load Alleviation in Aircraft Pre-design and Its Influence on Structural Mass and Fatigue - DLR-FB-2020-47," Ph.D. thesis, TU Berlin, Göttingen, https://elib.dlr.de/139558/, 2020.

[27] Bauknecht, A., Beyer, Y., Schultz, J., Asaro, S., Khalil, K., Römer, U., Steen, M., Cavaliere, D., and Fezans, N., "Novel Concepts for Active Load Alleviation," *AIAA SCITECH 2022 Forum*, San Diego, CA, USA & Virtual, 2021. https://doi.org/10.2514/6.2022-0009.

[28] Leishman, J., and Nguyen, K., "State-space representation of unsteady airfoil behavior," *AIAA Journal*, Vol. 28, No. 5, 1990, pp. 836–844. https://doi.org/10.2514/3.25127.

[29] Van Dam, C., "The aerodynamic design of multi-element high-lift systems for transport airplanes," *Progress in Aerospace Sciences*, Vol. 38, No. 2, 2002, pp. 101–144. https://doi.org/10.1016/S0376-0421(02)00002-7.

[30] Goitia, H., and Llamas, R., "Nonlinear vortex lattice method for stall prediction," *MATEC Web Conf.*, Vol. 304, 2019, p. 02006. https://doi.org/10.1051/matecconf/201930402006.

[31] Besselink, B., Tabak, U., Lutowska, A., van de Wouw, N., Nijmeijer, H., Rixen, D. J., Hochstenbach, M., and Schilders, W., "A comparison of model reduction techniques from structural dynamics, numerical mathematics and systems and control," *Journal of Sound and Vibration*, Vol. 332, No. 19, 2013, pp. 4403–4422. https://doi.org/10.1016/j.jsv.2013.03.025.

[32] Alder, M., Moerland, E., Jepsen, J., and Nagel, B., "Recent advances in establishing a common language for aircraft design with CPACS," *Aerospace Europe Conference 2020*, Bordeaux, France, Feb. 25–28, 2020.

[33] Heinrich, R., "Simulation of Interaction of Aircraft and Gust Using the TAU-Code," *New Results in Numerical and Experimental Fluid Mechanics IX*, Notes on Numerical Fluid Mechanics and Multidisciplinary Design, Vol. 124, edited by A. Dillmann, G. Heller, E. Krämer, H.-P. Kreplin, W. Nitsche, and U. Rist, Springer International Publishing, Cham, 2014, pp. 503–511. https://doi.org/10.1007/978-3-319-03158-3_51.